HHS Public Access

Author manuscript

Brain Behav Immun. Author manuscript; available in PMC 2025 January 01.

Published in final edited form as:

Brain Behav Immun. 2024 January ; 115: 131–142. doi:10.1016/j.bbi.2023.09.021.

Region-specific targeting of microglia *in vivo* using direct delivery of tamoxifen metabolites via microfluidic polymer fibers

Alexis M. Stranahan[1,*], **Anthony Tabet**[2], **Polina Anikeeva**[2,3]

[1]Department of Neuroscience and Regenerative Medicine, Medical College of Georgia, Augusta University, 1120 15th St, Augusta, GA 30912 USA

[2]Research Laboratory of Electronics and McGovern Institute for Brain Research, Massachusetts Institute of Technology, 77 Massachusetts Avenue, Cambridge, MA 02139-4307

[3]Departments of Materials Science & Engineering and Brain & Cognitive Sciences, Massachusetts Institute of Technology, 77 Massachusetts Avenue, Cambridge, MA 02139-4307

Abstract

Region-specific genetic manipulation of glial cells remains challenging due to the lack of anatomically selective transgenic models. Although local transduction is achievable with viral vectors, uniform recombination can be challenging in larger brain regions. We investigated the efficacy of intraparenchymal delivery of the tamoxifen metabolite endoxifen using inducible cre reporter mice. After observing localized reporter induction following stereotaxic injections of endoxifen in CX3CR1creERT2 mice, we carried out chronic delivery via osmotic pumps attached to bilateral cannulas made of stainless steel or microfluidic polymer fibers. Analysis of reporter expression in sections or iDISCO-cleared brains from TMEM119creERT2 mice revealed widespread induction following chronic infusion. Neuronal damage and gliosis were more prevalent around steel cannulas than polymer fibers, and glial reactivity was further attenuated when devices were implanted two months before drug delivery. In summary, region-specific recombination is achievable in glia with minimal tissue damage after endoxifen delivery via microfluidic polymer implants.

Keywords

Neurotechnology; Microfluidics; Microglia; Astrocyte; Tamoxifen; Endoxifen

Basic research in neurobiology has always relied heavily on invasive methods, such as stereotaxic injections or electrode and silica fiber optic implants (Lacour et al, 2016). Translational neuroscience also incorporates invasive methods, such as deep brain

[*]Corresponding Author: Alexis M. Stranahan, Ph.D., Department of Neuroscience and Regenerative Medicine, Medical College of Georgia, Augusta University, 1120 15th St, CA3009, Augusta, GA 30912 USA, Ph: (706) 721-7885, Fax: (706) 434-7823, astranahan@augusta.edu.

Conflict of interest statement: The authors have declared no conflict of interest exists.

stimulation and implanted electrode arrays that detect activity and deliver drugs to suppress epileptiform activity (Polikov et al, 2005). All of the above techniques involve acute mechanical injury, followed by chronic adaptations to foreign material, punctuated by sporadic microtraumas due to normal motion of the brain inside the skull (Lacour et al, 2016; Savya et al, 2022). The geometry, biomechanics, and surface chemistry of implanted materials regulate local tissue damage, glial scarring, and non-self recognition by microglia. Implants with mechanical properties approximating those of brain tissue typically evoke less damage than stiffer implants, enabling drug delivery, electrophysiological recording, and optogenetic stimulation of neurons over extended timeframes (Tabet et al, 2021; Park et al, 2017). The reductions in tissue trauma and immunogenicity of flexible materials also open exciting new avenues for research on glial biology, which has historically been constrained by the limited range of strategies for spatially restricted manipulation.

Regional heterogeneity in the onset and progression of glial activation is often assumed, but empirical data are scarce, and the lack of experimental approaches for anatomically selective gene deletions represents a major conceptual hurdle. Selective cre drivers for microglia have only recently become available (Kaiser and Feng, 2019; McKinsey et al, 2020), and while these models represent an advance over previous models targeting microglia and macrophages, gene deletions still impact microglia throughout the brain and spinal cord. Region-specific promoters have yet to be identified for microglia, which are notoriously difficult to transfect using viral vectors, especially in larger brain regions (Maes et al, 2019). Given the compartmentalized functional architecture of the CNS, region-specific approaches are critical to rigorously delineate microglial regulation of specific circuits and behaviors. These questions can only be answered with methods that elicit temporally controlled recombination in individual brain regions.

Directed expression of cre recombinase fused to a mutated estrogen receptor sequence (creER) is the most widely used strategy for inducible genetic manipulation *in vivo* (Feil et al, 1996). Early creER constructs retained sensitivity to endogenous estrogens, but subsequent generations introduced mutations that suppressed estrogen responsiveness while maintaining high affinity for synthetic steroids (Whitfield et al, 2015). The synthetic estrogen receptor modulator tamoxifen acts as a prodrug for metabolites that bind to the ER domain of creER with up to 100-fold greater affinity than tamoxifen itself (Reid et al, 2014; Johnson et al, 2004; Felker et al, 2016). Although tamoxifen is brain-penetrant, the enzymes required for oxidative breakdown of tamoxifen are not widely expressed in the nervous system (Lein et al, 2007; Jayaraman et al, 2021). Endoxifen and other metabolites released following hepatic breakdown of tamoxifen have successfully been delivered into the brain for local manipulation of astrocytes and vascular mural cells (Benedykcinska et al, 2016; Scherschinski et al, 2023), but microglia have yet to be targeted using this approach. We therefore optimized and validated methods for region-specific delivery of endoxifen using flexible microfluidic fibers that elicit minimal tissue damage. After optimizing delivery strategies, we determined the appropriate temporal windows to maximize immunological cloaking of implanted devices. These findings indicate that region-specific microglial recombination is achievable without widespread injury in the CNS.

Methods

Mouse models and experimental design

Mice were purchased from Jackson Labs or imported and bred in-house for these studies. Reporter mice were generated by crossing the floxed tdTomato reporter line Ai14 (Jax strain #007914) with mice expressing creERT2 under the myeloid-lineage promoter CX3CR1 (CX3CR1$^{cre/ERT2}$; Jax strain #021160), the excitatory neuron promoter Camk2a (Camk2a$^{cre/ERT2}$; Jax strain #012362), or the microglia-specific TMEM119 promoter (TMEM119$^{cre/ERT2}$; Jax strain #031820). Animals were housed in a ventilator rack on Alpha-dry bedding in a specific pathogen-free facility with food and water available ad libitum.

Experiment 1 compared reporter induction and local tissue damage after systemic tamoxifen (2.0mg/kg, 3x48hr, PO) or stereotaxic delivery of the tamoxifen metabolite Z-endoxifen (catalog#SML2368; Sigma-Aldrich, St. Louis, MO USA), as shown (Fig.1A). Experiment 2 compared outcomes after chronic intrahippocampal infusions of Z-endoxifen via steel cannulas or microfluidic polymer fibers (Fig.1B). In Experiment 2, cannulas or polymer fibers were connected to osmotic pumps and implanted when mice were four months old ('Single-stage surgery'). For Experiment 3, cannulas or polymer fibers were implanted into the hippocampus of two-month-old mice, and osmotic pumps were implanted in a separate surgery when mice were four months old ('Two-stage surgery') (Fig.1C). For all surgeries, mice were treated with Buprenorphine SR (1.0mg/kg) to alleviate postoperative distress. All mice were weighed at surgery, then weekly thereafter, and any mouse that lost >15% of its presurgical body weight was removed from the study.

Drug preparation and delivery

For intrahippocampal delivery in Experiment 1, endoxifen was reconstituted at 2mg/mL in dimethyl sulfoxide (DMSO; Benedykcinska et al, 2016) and 1.0μL was infused bilaterally at the following stereotaxic coordinates (AP-1.94, ML±2.0, DV-2.0; Paxinos and Franklin, 2003). Additional groups of mice received intrahippocampal injections of artificial cerebrospinal fluid (ACSF) or tamoxifen (2.0μg/μl, 1μl/side) at concentrations that mimic CNS bioavailability after systemic administration (Jahn et al, 2018). Stereotaxic injections were performed on a Kopf stereotaxic frame equipped with a Neuros syringe (Hamilton Company, Reno, NV USA) using a constant flow of 0.2μl/min, with the syringe left in place for ten minutes after administration.

For chronic infusion (Experiments 2-3), endoxifen was diluted to 167ng/microliter in ACSF (final concentration of DMSO=8%). Osmotic minipumps (Alzet model 1007D; Durect Corporation, Cupertino, CA, USA) were weighed before and after loading with endoxifen. Osmotic pumps were visually inspected at sacrifice before being cleaned, dried, and weighed to verify delivery.

Fabrication of infusion devices

Polymer-based microfluidic infusion devices were prepared as previously reported (Tabet et al, 2021). Briefly, polycarbonate rods were machined and drawn into fibers (OD=200

microns, ID=90 microns; Supplementary Fig.1). Fibers were inserted into commercially available bilateral cannulas (Plastics One 3220PD, cut 0.5mm below pedestal) using a 3D printed alignment tool (downloadable as Supplementary Data). Two small beads of optical epoxy were applied with the tip of a 29g needle to bond each polymer fiber to the stainless steel. Care was taken as too little epoxy resulted in poor bonding and leakage of fluid from the steel stub, and too much clogged the polymer implant inside the stub. Devices were UV-cured overnight, followed by thorough washing with isopropyl alcohol to test the integrity of each fluidic before implantation. Bilateral steel cannulas were purchased from Plastics One (Plastics One 3280PD, cut 2.0mm below pedestal; OD=360 microns, ID=180 microns). The bending stiffness of each implant was calculated using Young's modulus=2.38 gigapascals (GPa) for polycarbonate or 193GPa for steel, as described (Tabet et al, 2021). The calculated bending stiffness of polycarbonate fibers was 159.3 newtons/m (N/m) and 1.326×10^5 N/m for steel.

Assembly and implantation of infusion devices

For single-stage surgery (Experiment 2), osmotic pumps were loaded with Z-endoxifen and primed by immersion in sterile saline, as shown (Fig.2A). Osmotic pumps were then connected to the infusion devices using polyethylene tubing (Fig.2B-C) as previously reported (Wosiski-Kuhn et al, 2014; Erion et al, 2014; Dey et al, 2017). For surgery, mice were anesthetized with Isoflurane and mounted in a stereotaxic frame (Kopf Instruments). Scalp incisions were made above bregma and the drill was positioned at the following stereotaxic coordinates (AP-1.94, ML±2.0; Paxinos and Franklin, 2003). After drilling bilateral burr holes and confirming hemostasis, steel cannulas or microfluidic probes were positioned over the holes and lowered into place, as shown (Fig.2D). The base of the implanted device was secured to the skull using dental cement. While the dental cement was curing, the scalp incision was extended caudally to just above the scapulae (Fig.2D). Incisions were lavaged with sterile saline and blunt hemostats were used to create a subcutaneous pocket for the osmotic minipumps. The pumps were placed into the pocket and the tubing connecting each pump to the cannula was visually inspected for damage or introduction of bubbles. After confirming integrity, the skin incision was closed over the tubing with Surgibond tissue adhesive.

For two-stage surgery (Experiment 3), infusion devices were prefilled with ACSF and capped to maintain patency before being implanted into the hippocampus. Two months after the initial surgery, mice were anesthetized and an incision was made from the base of the skull to the scapulae, exposing the capped intake ports. Caps were removed and replaced with pre-assembled tubing attached to osmotic pumps. After connecting the tubing to the intake ports, minipumps were inserted subcutaneously and enclosed beneath the skin as described for single-stage surgery.

Immunofluorescence and quantitative morphometry in brain sections

In Experiments 1-2, mice were sacrificed by transcardial perfusion with 4% paraformaldehyde in phosphate buffer (PFA). Brains were then postfixed overnight and dehydrated in 30% sucrose before being snap-frozen on dry ice. In Experiment 1, sagittal sections were cut in a 1:4 series at 40micron thickness on a freezing microtome (Leica). In

Experiment 2, coronal sections were prepared as a 1:6 series at 40 micron thickness. The number and spacing between sections was recorded and only samples with intact spacing were used for quantification. Free-floating sections were processed for immunodetection of IBA1 or GFAP, or mounted on slides for Fluoro Jade histochemistry, as described (Manzanero et al, 2014; Hao et al, 2016; Yamamoto et al, 2019). To ensure appropriate spacing, the number of sections was recorded at the start and end of each reaction. Sections were mounted on Superfrost Plus slides in rostrocaudal order and nuclei were counterstained with DAPI prior to imaging.

Montage images of brain sections were acquired on a Zeiss MTB epifluorescence microscope with a motorized stage in Microlucida software (Microbrightfield, Williston, VT). After identifying implant or injection sites based on DAPI counterstaining and tdTomato fluorescence, densitometric analysis of IBA1 and GFAP was carried out in manually segmented regions of interest (ROIs) over the hippocampus. Z-stacks were subsequently acquired at regular intervals from the placement site on a Zeiss 780 confocal microscope for analysis of gliosis, colocalization, or dendritic spine densities according to published methododology (Guo et al, 2020; Erion et al, 2014; Stranahan, 2011).

Tissue processing and immunodetection in cleared brains

In Experiment 3, hemibrains were processed using iDISCO (Renier et al, 2014), with minor modifications for immunodetection of GFAP. In brief, samples were dehydrated through increasing concentrations of methanol (MeOH), delipidated in dichloromethane (DCM), bleached in hydrogen peroxide, and rehydrated through decreasing concentrations of methanol according to the original iDISCO protocol (Renier et al, 2014). Brains were then blocked and permeabilized in PBS containing 6.0% normal donkey serum (v/v), 2.0% Triton-X 100 (v/v), 10% DMSO (v/v), and 10% glycine (w/vol) for 1hr at RT, followed by another 1hr at 60C in the same buffer. After blocking and temperature-enhanced permeabilization, brains were incubated in Alexa Fluor 647-conjugated anti-GFAP (1:200, Biolegend cat#837512) and rabbit anti-RFP/tdTomato (1:200, Rockland cat#600-401-379) in the same buffer, omitting glycine, for 7d at 37C. Samples were then washed 3x3hr, then overnight, in the same wash buffer described in Renier et al (2014) before being incubated with secondary antibody Alexa Fluor 546-conjugated donkey anti-rabbit (1:500) according to the published iDISCO protocol. Immunodetection of IBA1 and tdTomato was carried out according to published iDISCO protocols using rabbit anti-IBA1 (1:500; Wako cat#019-19741) and goat anti-RFP/tdTomato (1:500, Rockland cat#200-101-379). After washes, IBA1 was detected using Alexa 647 donkey anti-rabbit and tdTomato was visualized with Alexa 546 donkey anti-goat (both at 1:500). After additional washes, samples were dehydrated through methanol, delipidated in DCM, and cleared in dibenzyl ether (DBE), as reported (Renier et al, 2014).

Light-sheet image acquisition, processing, and analysis

Brains were imaged in SuperPlan configuration on a LaVision Ultramicroscope II (Miltenyi). Tiles were acquired with a nominal XY resolution of 0.37px/micron and stitched using Terastitcher (Bria et al, 2012). Autofluorescence images (488ex/525±50em) were subtracted from images of tdTomato (561ex/620±60em) and IBA1 or GFAP

(647ex/680±30em) and used to calculate transformation onto the Allen Brain Atlas in Neuroinfo software (Microbrightfield, Williston, VT). Transforms calculated from the corresponding autofluorescence images were applied to images of tdTomato, IBA1, and GFAP. Autofluorescence images were then converted to 8bit and imported into Reconstruct (Fiala, 2005; freely available at https://synapseweb.clm.utexas.edu) for semiautomatic tracing of cannula tracks. Track areas were subtracted from total sample areas on each optical slice, generating adjusted sample areas for normalization of tdTomato+ cell counts and immunoreactivity for IBA1 or GFAP.

tdTomato+ cells were quantified in NeuroInfo after conversion to 8bit for ease of file handling. Images of IBA1 and GFAP were analyzed in native 16bit format after Otsu thresholding in Fiji/ImageJ, as described (Yamamoto et al, 2019; Stranahan et al, 2023). For first-pass analysis, suprathreshold labeling area was determined around each cannula track and expressed relative to adjusted sample area. To analyze anatomical gradients in immunoreactivity for IBA1 and GFAP, we modified previously reported methods for multichannel Sholl analysis (Hao et al, 2016). Two-dimensional cannula track tracings were overlaid on the corresponding images of IBA1 or GFAP in Meshlab (freely available at https://www.meshlab.net/) and scaled in 100 micron increments to generate concentric traces. Toroid regions of interest (ROIs) were generated using adjacent pairs of concentric traces for analysis of IBA1 or GFAP immunoreactivity at 100 micron intervals around each cannula track. Suprathreshold labeling area in each ROI was subsequently normalized to values from the first 100 micron toroid around the border of each cannula track to generate a size-independent measure of anatomically graded gliosis surrounding each implant. Group differences were determined within the boundaries of the hippocampus, as defined by the Allen Brain Atlas Common Coordinate Framework. For analysis along the dorsoventral axis of the cannula track, the overlying cortical regions were included and anatomical boundaries are noted in the appropriate figure legends.

Statistics

For stereotaxic injections, data were analyzed using one-way ANOVA with Tukey's post hoc. For single-stage surgery in Camk2a^{creERT2}/tdTomato$^{fl/fl}$ mice, dendritic spine densities were analyzed using t-tests and cell counts were analyzed using one-way ANOVA with Tukey's post hoc. For single-stage surgery in TMEM119^{creERT2}/tdTomato$^{fl/fl}$ mice, densitometric and morphological measures were compared across mice that received stereotaxic injection, steel cannulas, or microfluidic fiber implants using one-way ANOVA with Tukey's post hoc. For two-stage surgery, tdTomato+ cell counts, track volumes, and total immunoreactivity for glial markers was analyzed using t-tests. Anatomical gradients in immunoreactivity were analyzed using linear regression and compared between different implant types using one-way repeated-measures ANOVA with Tukey's post hoc. All analyses were carried out with statistical significance at $p<0.05$ in Graphpad Prism version 9.0.

Results

Local infusions of tamoxifen metabolites induce cre reporter expression

We initially compared tdTomato induction in 8-10wk old CX3CR1^{creERT2} reporter mice after intrahippocampal administration of Z-endoxifen, tamoxifen, or ACSF (Fig.1A). Bilateral stereotaxic injections were delivered using a stainless steel microsyringe. Intrahippocampal delivery of endoxifen induced tdTomato expression (Fig.3A), but reporter induction after intrahippocampal tamoxifen did not differ from ACSF (Fig.3A-B), as predicted by the absence of enzymes required for local generation of tamoxifen metabolites (Fig.1A; Lein et al, 2007; Jayaraman et al, 2021). Tissue damage was assessed based on Fluoro Jade histochemistry, which revealed sparse nuclei around the injection site (Fig.3C-D). There was no difference in the number of Fluoro Jade+ nuclei after intrahippocampal endoxifen, tamoxifen, or ACSF (Fig.3D). There were also no differences in weight gain after stereotaxic injections of endoxifen, tamoxifen, or ACSF (weight change [g], mean ± SEM, n=6/condition; endoxifen = 0.16 ± 0.04; tamoxifen = 0.13 ± 0.07; ACSF = 0.18 ± 0.05). These results indicate that intrahippocampal endoxifen activates creERT2, and that stereotaxic injections elicit localized cellular degeneration around the injection site.

Chronic infusion via microfluidic fiber implants elicits widespread reporter expression

Stereotaxic injections of endoxifen induced reporter expression, but tdTomato+ cells were only observed around the injection site. This anatomically restricted pattern led us to implement strategies for chronic intrahippocampal delivery of endoxifen. While repeated stereotaxic injections can be performed into the same brain region, we sought to minimize mechanical trauma by infusing endoxifen into the hippocampus via osmotic pumps. To evaluate local tissue damage and reporter induction in excitatory neurons, hemizygous Camk2a^{creERT2} reporter mice received 1wk infusions into the hippocampus via bilateral steel cannulas or microfluidic polymer fibers (Fig.4A). Mice were sacrificed 2wk after surgery and complete delivery was verified based on pump weights at sacrifice (Supplementary Fig.2).

Stereological quantification of Fluoro Jade-stained nuclei revealed fewer damaged cells in mice that received polymer fibers (Fig.4B-C; $F_{2,20}$=13.2, p<0.01). Chronic delivery of endoxifen evoked tdTomato induction around the implants (Fig.4D), but tdTomato+ cell numbers were unaffected by implant type in CA1 (% tdTomato+, mean±SEM, n=6/condition; fiber=16.9±1.8; steel=16.4±2.15) and in the dentate gyrus (fiber=15.6±1.6; steel=14.2±1.4). tdTomato+ cells adjacent to the implant site lacked processes and exhibited nuclear condensation (Fig.4E), but neuronal morphology distal to the implant site was comparable to published reports in Camk2a reporter mice (Chakravarthy et al, 2006; Veldman et al, 2020). Camk2a is widely expressed throughout the dendritic arbor and at dendritic spines, enabling their visualization in Camk2a reporter lines (Chakravarthy et al, 2006). Dendritic spine density along the apical oblique dendrites of CA1 neurons distal to the implant site was unaffected by implant type (Fig.4F-G), and spine densities in the dentate molecular layer were also similar between groups (Fig.4F,H). These observations indicate that polymer fiber implants elicit less cell death than steel cannulas at the placement site without detectable alterations in dendritic spines at distal sites. Together with published

data demonstrating improved synaptic function in mice with polymer fiber implants (Tabet et al, 2021; Park et al, 2017), these data indicate that flexible materials reduce mechanical trauma.

Chronic central infusions of endoxifen and effects of implant material on glial reactivity

The CX3CR1^{creERT2} model exhibits recombination in circulating myeloid cells and in peripheral tissues, as well as in the nervous system (Parkhurst et al, 2013). At extended periods after induction, recombination is limited to slower-cycling microglia and long-lived 'border-associated macrophages' in the choroid plexus and perivascular space (Parkhurst et al, 2013; Goldmann et al, 2016). To determine whether central endoxifen delivery might be an effective strategy for targeting microglia, we carried out chronic intrahippocampal infusions in mice expressing tdTomato under the microglia-specific TMEM119 promoter (Bennett et al, 2016; Kaiser and Feng, 2019). Reporter induction, gliosis, and local tissue damage were compared in TMEM119creERT2 reporter mice after stereotaxic injection or chronic infusion via microfluidic polymer fibers or steel cannulas, as shown (Fig.5A). There were no differences in weight gain over the 2wk period after surgery (Supplementary Fig.3A-B), and pump weights were comparably reduced after infusion via steel cannulas or fiber probes (Supplementary Fig.2). Native tdTomato fluorescence and IBA1 immunoreactivty were visualized on serial coronal sections (Fig.5B-C). Quantification of tdTomato+ cells revealed more widespread recombination after chronic delivery than after stereotaxic injection (Fig.5D; $F_{2,45}$=26.4, p<0.01), and analysis of IBA1/tdTomato colabeling revealed anatomically graded reporter induction around the implant site (Fig.5E). When co-labeling was averaged across all distances from the implant site, mice that received polymer fiber implants had significantly more double-labeled cells than mice with steel implants (Fig.5E; $F_{2,15}$=14.9, p<0.01). Polymer fibers also evoked smaller increases in IBA1 staining area at the placement site, relative to steel cannulas (Fig.5F; $F_{2,15}$=16.2, p<0.01). However, both implants increased IBA1 immunoreactivity more than single stereotaxic injections (Fig.5F).

Visualization of GFAP and tdTomato in an adjacent series of serial sections revealed no evidence of reporter expression in astrocytes (Fig.5G-H), consistent with expression patterns reported after systemic delivery of tamoxifen in TMEM119 reporter mice (Kaiser and Feng, 2019). Although chronic infusion increased GFAP immunoreactivity more than stereotaxic injection, increases were more widespread in mice that received steel cannulas, relative to mice with polymer fiber implants (Fig.5G-H; $F_{2,15}$=23.4, p<0.01). Differences in gliosis were not due to the mechanical effects of continuous infusion, as analysis of GFAP and IBA1 immunoreactivity in mice with implants that were not connected to osmotic pumps revealed no difference relative to mice that received infusions (Supplementary Fig.4A-B). These observations indicate that chronic infusions of endoxifen via microfluidic polymer fibers elicits widespread recombination and causes less damage than steel cannulas after single-stage implantation in adult mice.

Reductions in microglial activation following central delivery of endoxifen via polymer fibers

To allow more time for parenchymal acclimation, we implanted microfluidic polymer fibers or steel cannulas in 8wk old TMEM119^{creERT2}/tdTomato$^{fl/fl}$ mice (Fig.6A). Two months after the initial surgery, the intake ports were attached to osmotic pumps for delivery of Z-endoxifen (Fig.6A). After confirming delivery based on pump weights, brains were processed for iDISCO clearing and immunodetection (Fig.6B). Cannula tracks were traced on stitched z-stack images and the volume of each track was calculated from 3D reconstructions (Fig.6C). Cannula track areas were subtracted from total sample areas on each optical slice (Fig.6C), generating adjusted sample areas for normalization. tdTomato+ cell numbers were quantified on each optical slice and expressed relative to adjusted sample area (Fig.6D). Images of GFAP or IBA1 were acquired in parallel with images of tdTomato from each sample (Fig.6E-F). After stitching and autofluorescence correction, z-stacks were thresholded for analysis of suprathreshold staining area. For insight into anatomically graded gliosis along with anteroposterior and mediolateral axes, we modified the multichannel Sholl analysis used in our previous publication (Hao et al, 2016). Two-dimensional cannula track traces were overlaid on the corresponding images of IBA1 and scaled up in 100 micron increments, generating concentric traces around each placement site (Fig.6G). Adjacent pairs of traces were used to delineate toroid regions of interest (ROIs) for analysis of IBA1 immunoreactivity (Fig.6G). Except where noted, measurements were generated within the boundaries of the hippocampus as defined the the Allen Brain Atlas Common Coordinate Framework (Fig.6H).

This analysis revealed comparable recombination efficacy after endoxifen infusion through polymer fibers or stainless steel cannulas, as reflected by similar tdTomato+ cell numbers (Fig.7A-C). Off-target anatomical effects were minimal, as quantification of tdTomato+ cells on individual optical slices revealed limited induction in overlying cortex (Fig.7D). Consistent with the different geometries of each implant, cannula track volumes were larger in mice that received steel cannulas, as opposed to polymer fibers (t_{17}=3.9, p<0.01; Supplementary Fig.5). To control for these differences, track areas were subtracted from total sampled area, generating adjusted values for normalization of tdTomato+ cell counts and immunoreactivity for IBA1 or GFAP.

Analysis of IBA1 immunoreactivity revealed lower suprathreshold staining areas along the dorsoventral extent of the track left behind by polymer fiber implants (Fig.7E). Reductions were evident from the cortical surface to the hippocampus (Fig.7F; t_{17}=4.1, p<0.01), as reflected by average suprathreshold labeling area. Sholl analysis revealed declines in IBA1 staining area with increasing distance from the cannula track left by polymer fiber implants (Supplementary Fig.6A; R^2=0.82, p<0.01). By contrast, IBA1 staining area remained consistently elevated at all intervals around steel cannulas (Supplementary Fig.6A; R^2=0.09, n.s.). Differences were statistically significant when suprathreshold labeling areas were analyzed with repeated-measures ANOVA (Fig.7G; $F_{4,56}$=20.3, p<0.01), and linear slopes representing IBA1 immunoreactivity as a function of distance were also significantly different between groups (Supplementary Fig.6A-B; $F_{1,76}$=30.2, p<0.01). This relationship was upheld after normalizing the data to initially measured immunoreactivity within 100

microns of the track border (Fig.7H; $F_{4,56}$=34.7, p<0.01), indicating that flexible polymer fibers elicit less microglial reactivity than steel cannulas along all measured anatomical axes.

Steel cannulas elicit more widespread astrogliosis than polymer fibers

Microglia play a critical role in removing dead cells, while astrocytes surround and encapsulate injured tissue (Silver and Miller, 2004). For insight into astrogliosis after two-stage surgery, we visualized GFAP 2wk after connecting osmotic minipumps to intrahippocampal delivery devices implanted at 8wk old, as shown (Fig.1C). GFAP immunoreactivity was elevated throughout the dorsoventral extent of cannula tracks from steel implants, relative to microfluidic polymer fibers (Fig.8A-C; t_{17}=4.9, p<0.01). This difference was evident throughout the dorsoventral extent of the cannula track from the cortical surface to the hippocampal parenchyma (Fig.8D). Sholl analysis of GFAP immunoreactivity was carried out in toroid ROIs centered on the cannula track, as shown for IBA1 (Fig.6G). These data revealed declining immunoreactivity around polymer fiber implants, but not steel cannulas (Fig.8E; $F_{4,56}$=18.9, p<0.01). The same pattern was evident when GFAP staining area was normalized to the initial ROI, 100 microns around the border of the cannula track (Fig.8F; $F_{4,56}$=27.0, p<0.01). Taken together, these data indicate that delivery of endoxifen via microfluidic fibers elicits region-specific recombination in glia with minimal damage to the surrounding environment.

Discussion

Here, we report that intraparenchymal delivery of tamoxifen metabolites is an effective strategy for region-specific targeting of microglia. Local infusions of the tamoxifen metabolite Z-endoxifen induced hippocampal reporter expression in multiple lines of inducible cre mice. Chronic infusions were more effective than stereotaxic injection, but also evoked widespread damage when administered via indwelling steel cannulas. Intrahippocampal administration using microfluidic polymer fibers induced widespread recombination with less damage, especially when polymer fiber devices were implanted and allowed to acclimate for extended periods before drug delivery. Delivery of creERT ligands using flexible microfluidic fibers therefore enables region-specific genetic manipulation of cells in the brain parenchyma with limited glial activation or neurodegeneration.

This report builds on functional improvements in mice with flexible implants reported in previously published work (Canales et al, 2015; Park et al, 2017; Park et al. 2021). Specifically, stable synaptic recordings were performed up to six months after surgery in mice with flexible implants, which exceeds the typical timeframe for high-fidelity recording in mice with traditional implants (Canales et al, 2015; Park et al, 2017; Park et al. 2021). Polymer fiber implants also elicit less damage to the blood-brain barrier than similarly-sized steel wires (Park et al, 2017). While cytokine levels were not directly quantified in the current study, the differences in immunoreactivity strongly suggest that local inflammatory responses were reduced. Conclusions regarding neuroinflammation are routinely based on immunoreactivity for glial antigens in preclinical studies. When interpreted relative to published electrophysiological data from the Anikeeva lab (Canales et al, 2015; Park et

al, 2017; Park et al. 2021), the current report indicates that polymer fibers elicit less damage than traditional steel cannulas.

Microglial activation following mechanical trauma occurs in parallel with encapsulation of the injured region by astrocytes, forming the glial scar (Silver and Miller, 2004). Unlike peripheral scar tissue, which becomes stiffer after resolution of injury, glial scars in the CNS exhibit localized increases in tissue elasticity (Moeendarbary et al, 2017; Silver and Miller, 2004). Paradoxically, softening of the extracellular matrix due to glial scarring around steel implants could predispose the local environment to repeated mechanical trauma. Microfluidic polymer probes are more flexible than steel, which improves their ability to move with the dynamic motions of the brain inside the skull (Frank et al, 2019). Stainless steel implants elicit greater microglial and astrocytic activation compared to soft polymer probes with identical dimensions (Canales et al, 2015; Park et al, 2017). This is underscored by Sholl analysis of glial reactivity at fixed intervals around each implant, which revealed steeper declines with increasing distance from polymer implants. Prior work also suggests that glial responses to both rigid and flexible implants decrease over time (Park et al, 2017; Park et al, 2021). Duration-dependent accommodation of implanted devices was also evident in the current report, based on the more dramatic reductions in gliosis observed when placement of intrahippocampal implants was carried out two months before drug delivery. Polymer-based microfluidic devices maintain their patency and are capable of intrathecal delivery chronically in vivo (Tabet et al, 2021). Multifunctional fiber implants have also been used successfully in the prefrontal cortex, basolateral amygdala, spinal cord, and nucleus accumbens (Canales et al, 2015; Park et al, 2017; Park et al, 2021; Tabet et al, 2021). The results of this study support the robustness of this delivery platform and suggest that flexible devices enable stealthy in vivo manipulation of microglia.

Bioavailability of tamoxifen metabolites in the CNS peaks 2-4d after peripheral administration of tamoxifen (Jahn et al, 2018), resulting in persistent cre-mediated recombination. Stereotaxic injections of endoxifen into the cerebral ventricles induced astroglial reporter expression in GLASTcreERT mice, but was associated with varying levels of toxicity in a previous report (Benedykcinska et al, 2016). Benedykcinska et al (2016) administered (E/Z)-endoxifen hydrochloride hydrate, an approximately 1:1 mixture of the *cis*- (E) and *trans*- (Z) isomers of endoxifen (Elkins et al, 2014). Similar to tamoxifen, the (E) and (Z) isomers of endoxifen have distinct affinities and modulatory actions at estrogen receptors (Jayaraman et al, 2021; Jordan et al, 1988). (Z)-endoxifen is the biologically active isomer with estrogen receptor binding affinities similar to tamoxifen, while (E)-endoxifen exhibits weak estrogenic activity (Elkins et al, 2014). We detected no evidence of toxicity following intrahippocampal delivery of the (Z)-isomer in these studies, suggesting that the adverse physiological effects reported by Benedykcinska et al (2016) could be due to the (E)-isomer.

In this study, chronic infusions of endoxifen induced reporter expression in approximately 30% of IBA1+ cells, which is within the range associated with biologically significant effects observed using AAV in hypothalamic astrocytes (García-Cáceres et al, 2016). However, the hippocampus is considerably larger than the hypothalamic nuclei targeted in previous work (García-Cáceres et al, 2016). Penetrance and efficacy continue to

present technical challenges for studies of glial biology, and future animal models with combinatorial genetic targeting could eventually overcome these issues. At present, the current results indicate that intraparenchymal delivery of tamoxifen metabolites is an effective and complementary strategy for region-specific manipulation of glial cells in the adult brain.

Supplementary Material

Refer to Web version on PubMed Central for supplementary material.

Acknowledgements:

This research was supported by R01DK110586 (A.M.S.), by a Paul and Daisy Soros Fellowship to A.T, and by funding from the McGovern Institute for Brain Research (P.A).

References

Benedykcinska A, Ferreira A, Lau J, Broni J, Richard-Loendt A, Henriquez NV, Brandner S Generation of brain tumours in mice by Cre-mediated recombination of neural progenitors in situ with the tamoxifen metabolite endoxifen. Dis Model Mech. 2016 Feb;9(2):211–20. [PubMed: 26704996]

Bennett ML, Bennett FC, Liddelow SA, Ajami B, Zamanian JL, Fernhoff NB, Mulinyawe SB, Bohlen CJ, Adil A, Tucker A, Weissman IL, Chang EF, Li G, Grant GA, Hayden Gephart MG, Barres BA. New tools for studying microglia in the mouse and human CNS. Proc Natl Acad Sci U S A. 2016 Mar 22;113(12):E1738–46. [PubMed: 26884166]

Bria A, Iannello G. TeraStitcher - a tool for fast automatic 3D-stitching of teravoxel-sized microscopy images. BMC Bioinformatics. 2012 Nov 27;13:316. [PubMed: 23181553]

Canales A, Jia X, Froriep UP, Koppes RA, Tringides CM, Selvidge J, Lu C, Hou C, Wei L, Fink Y, Anikeeva P. Multifunctional fibers for simultaneous optical, electrical and chemical interrogation of neural circuits in vivo. Nat Biotechnol. 2015 Mar;33(3):277–84. [PubMed: 25599177]

Chakravarthy S, Saiepour MH, Bence M, Perry S, Hartman R, Couey JJ, Mansvelder HD, Levelt CN. Postsynaptic TrkB signaling has distinct roles in spine maintenance in adult visual cortex and hippocampus. Proc Natl Acad Sci U S A. 2006 Jan 24;103(4):1071–6. [PubMed: 16418274]

Dey A, Hao S, Wosiski-Kuhn M, Stranahan AM. Glucocorticoid-mediated activation of GSK3β promotes tau phosphorylation and impairs memory in type 2 diabetes. Neurobiol Aging. 2017 Sep;57:75–83. [PubMed: 28609678]

Elkins P, Coleman D, Burgess J, Gardner M, Hines J, Scott B, Kroenke M, Larson J, Lightner M, Turner G, White J, Liu P. Characterization of the isomeric configuration and impurities of (Z)-endoxifen by 2D NMR, high resolution LCMS, and quantitative HPLC analysis. J Pharm Biomed Anal. 2014 Jan;88:174–9. [PubMed: 24055701]

Erion JR, Wosiski-Kuhn M, Dey A, Hao S, Davis CL, Pollock NK, Stranahan AM. Obesity elicits interleukin 1-mediated deficits in hippocampal synaptic plasticity. J Neurosci. 2014 Feb 12;34(7):2618–31. [PubMed: 24523551]

Felker A, Nieuwenhuize S, Dolbois A, Blazkova K, Hess C, Low LW, Burger S, Samson N, Carney TJ, Bartunek P, Nevado C, Mosimann C. In Vivo Performance and Properties of Tamoxifen Metabolites for CreERT2 Control. PLoS One. 2016 Apr 14;11(4):e0152989. [PubMed: 27077909]

Fiala JC. Reconstruct: a free editor for serial section microscopy. J Microsc. 2005 Apr;218(Pt 1):52–61. [PubMed: 15817063]

Frank JA, Antonini MJ, Anikeeva P. Next-generation interfaces for studying neural function. Nat Biotechnol. 2019 Sep;37(9):1013–1023. [PubMed: 31406326]

García-Cáceres C, Quarta C, Varela L, Gao Y, Gruber T, Legutko B, Jastroch M, Johansson P, Ninkovic J, Yi CX, Le Thuc O, Szigeti-Buck K, Cai W, Meyer CW, Pfluger PT, Fernandez AM, Luquet S, Woods SC, Torres-Alemán I, Kahn CR, Götz M, Horvath TL, Tschöp MH.

Astrocytic Insulin Signaling Couples Brain Glucose Uptake with Nutrient Availability. Cell. 2016 Aug 11;166(4):867–880. [PubMed: 27518562]

Goldmann T, Wieghofer P, Jordão MJ, et al. Origin, fate and dynamics of macrophages at central nervous system interfaces. Nat Immunol. 2016;17(7):797–805. [PubMed: 27135602]

Guo DH, Yamamoto M, Hernandez CM, Khodadadi H, Baban B, Stranahan AM. Beige adipocytes mediate the neuroprotective and anti-inflammatory effects of subcutaneous fat in obese mice. Nat Commun. 2021 Jul 30;12(1):4623. doi: 10.1038/s41467-021-24540-8. [PubMed: 34330904]

Guo DH, Yamamoto M, Hernandez CM, Khodadadi H, Baban B, Stranahan AM. Visceral adipose NLRP3 impairs cognition in obesity via IL-1R1 on CX3CR1+ cells. J Clin Invest. 2020 Apr 1;130(4):1961–1976. [PubMed: 31935195]

Hao S, Dey A, Yu X, Stranahan AM. Dietary obesity reversibly induces synaptic stripping by microglia and impairs hippocampal plasticity. Brain Behav Immun. 2015 Aug 31. pii: S0889-1591(15)30007-6. doi: 10.1016/j.bbi.2015.08.023. [Epub ahead of print]

Iusuf D, Teunissen SF, Wagenaar E, Rosing H, Beijnen JH, Schinkel AH. P-glycoprotein (ABCB1) transports the primary active tamoxifen metabolites endoxifen and 4-hydroxytamoxifen and restricts their brain penetration. J Pharmacol Exp Ther. 2011 Jun;337(3):710–7. [PubMed: 21378205]

Jahn HM, Kasakow CV, Helfer A, Michely J, Verkhratsky A, Maurer HH, Scheller A, Kirchhoff F. Refined protocols of tamoxifen injection for inducible DNA recombination in mouse astroglia.Sci Rep. 2018 Apr 12;8(1):5913. doi: 10.1038/s41598-018-24085-9. [PubMed: 29651133]

Jayaraman S, Reid JM, Hawse JR, Goetz MP. Endoxifen, an Estrogen Receptor Targeted Therapy: From Bench to Bedside. Endocrinology. 2021 Dec 1;162(12):bqab191. [PubMed: 34480554]

Johnson MD, Zuo H, Lee KH, Trebley JP, Rae JM, Weatherman RV, Desta Z, Flockhart DA, Skaar TC. Pharmacological characterization of 4-hydroxy-N-desmethyl tamoxifen, a novel active metabolite of tamoxifen. Breast Cancer Res Treat. 2004 May;85(2):151–9. [PubMed: 15111773]

Jordan VC, Koch R, Langan S, McCague R. Ligand interaction at the estrogen receptor to program antiestrogen action: a study with nonsteroidal compounds in vitro. Endocrinology. 1988 Apr;122(4):1449–54. [PubMed: 3345720]

Kaiser T, Feng G. Tmem119-EGFP and Tmem119-CreERT2 Transgenic Mice for Labeling and Manipulating Microglia. eNeuro. 2019 Aug 26;6(4):ENEURO.0448-18.2019.

Lacour SP, Courtine G, Guck J. Materials and technologies for soft implantable neuroprostheses. Nature Reviews Materials. 2016 Sep 27;1(10):1–4.

Lein ES, Hawrylycz MJ, Ao N, Ayres M, Bensinger A, Bernard A, Boe AF, et al. Genome-wide atlas of gene expression in the adult mouse brain. Nature. 2007 Jan 11;445(7124):168–76. [PubMed: 17151600]

Maes ME, Colombo G, Schulz R, Siegert S. Targeting microglia with lentivirus and AAV: Recent advances and remaining challenges. Neurosci Lett. 2019 Aug 10;707:134310. [PubMed: 31158432]

McKinsey GL, Lizama CO, Keown-Lang AE, Niu A, Santander N, Larpthaveesarp A, Chee E, Gonzalez FF, Arnold TD. A new genetic strategy for targeting microglia in development and disease. Elife. 2020 Jun 23;9:e54590. [PubMed: 32573436]

Moeendarbary E, Weber IP, Sheridan GK, Koser DE, Soleman S, Haenzi B, Bradbury EJ, Fawcett J, Franze K. The soft mechanical signature of glial scars in the central nervous system. Nat Commun. 2017 Mar 20;8:14787. [PubMed: 28317912]

Park S, Guo Y, Jia X, Choe HK, Grena B, Kang J, Park J, Lu C, Canales A, Chen R, Yim YS, Choi GB, Fink Y, Anikeeva P. One-step optogenetics with multifunctional flexible polymer fibers. Nature Neuroscience. 2017 Feb;20;612–619. [PubMed: 28218915]

Park S, Yuk H, Zhao R, Yim YS, Woldeghebriel EW, Kang J, Canales A, Fink Y, Choi GB, Zhao X, Anikeeva P. Adaptive and multifunctional hydrogel hybrid probes for long-term sensing and modulation of neural activity. Nat Commun. 2021 Jun 8;12(1):3435. [PubMed: 34103511]

Parkhurst CN; Yang G; Ninan I; Savas JN; Yates JR 3rd; Lafaille JJ; Hempstead BL; Littman DR; Gan WB. 2013. Microglia promote learning-dependent synapse formation through brain-derived neurotrophic factor. Cell 155(7):1596–609. [PubMed: 24360280]

Polikov VS, Tresco PA, Reichert WM. Response of brain tissue to chronically implanted neural electrodes. J Neurosci Methods. 2005 Oct 15;148(1):1–18. [PubMed: 16198003]

Reid JM, Goetz MP, Buhrow SA, Walden C, Safgren SL, Kuffel MJ, Reinicke KE, Suman V, Haluska P, Hou X, Ames MM. Pharmacokinetics of endoxifen and tamoxifen in female mice: implications for comparative in vivo activity studies. Cancer Chemother Pharmacol. 2014 Dec;74(6):1271–8. [PubMed: 25318936]

Renier N, Wu Z, Simon DJ, Yang J, Ariel P, Tessier-Lavigne M. iDISCO: a simple, rapid method to immunolabel large tissue samples for volume imaging. Cell. 2014 Nov 6;159(4):896–910. [PubMed: 25417164]

Savya SP, Li F, Lam S, Wellman SM, Stieger KC, Chen K, Eles JR, Kozai TDY. In vivo spatiotemporal dynamics of astrocyte reactivity following neural electrode implantation. Biomaterials. 2022 Oct;289:121784. [PubMed: 36103781]

Scherschinski L, Han C, Kim YH, Winkler EA, Catapano JS, Schriber TD, Vajkoczy P, Lawton MT, Oh SP. Localized conditional induction of brain arteriovenous malformations in a mouse model of hereditary hemorrhagic telangiectasia. Angiogenesis. 2023 May 23. doi: 10.1007/s10456-023-09881-w.

Silver J, Miller JH. Regeneration beyond the glial scar. Nat Rev Neurosci. 2004 Feb;5(2):146–56. [PubMed: 14735117]

Stranahan AM, Guo DH, Yamamoto M, Hernandez CM, Khodadadi H, Baban B, Zhi W, Lei Y, Lu X, Ding K, Isales CM. Sex Differences in Adipose Tissue Distribution Determine Susceptibility to Neuroinflammation in Mice With Dietary Obesity. Diabetes. 2023 Feb 1;72(2):245–260 [PubMed: 36367881]

Tabet A, Antonini MJ, Sahasrabudhe A, Park J, Rosenfeld D, Koehler F, Yuk H, Hanson S, Stinson J, Stok M, Zhao X, Wang C, Anikeeva P. Modular Integration of Hydrogel Neural Interfaces. ACS Cent Sci. 2021 Sep 22;7(9):1516–1523. [PubMed: 34584953]

Tabet A, Apra C, Stranahan AM, Anikeeva A. Changes in Brain Neuroimmunology Following Injury and Disease. Front Integr Neurosci. 2022 Apr 27;16:894500. [PubMed: 35573444]

Teft WA, Mansell SE, Kim RB. Endoxifen, the active metabolite of tamoxifen, is a substrate of the efflux transporter P-glycoprotein (multidrug resistance 1). Drug Metab Dispos. 2011 Mar;39(3):558–62. [PubMed: 21148080]

Veldman MB, Park CS, Eyermann CM, Zhang JY, Zuniga-Sanchez E, Hirano AA, Daigle TL, Foster NN, Zhu M, Langfelder P, Lopez IA, Brecha NC, Zipursky SL, Zeng H, Dong HW, Yang XW. Brainwide Genetic Sparse Cell Labeling to Illuminate the Morphology of Neurons and Glia with Cre-Dependent MORF Mice. Neuron. 2020 Oct 14;108(1):111–127.e6. [PubMed: 32795398]

Whitfield J, Littlewood T, Evan GI, Soucek L. The estrogen receptor fusion system in mouse models: a reversible switch. Cold Spring Harb Protoc. 2015 Mar 2;2015(3):227–34. [PubMed: 25734072]

Whitfield J, Littlewood T, Soucek L. Tamoxifen administration to mice. Cold Spring Harb Protoc. 2015 Mar 2;2015(3):269–71. [PubMed: 25734062]

Wosiski-Kuhn M, Bota M, Snider CA, Wilson SP, Venkataraju KU, Osten P, Stranahan AM. Hippocampal brain-derived neurotrophic factor determines recruitment of anatomically connected networks after stress in diabetic mice. Hippocampus. 2018 Dec;28(12):900–912. doi: 10.1002/hipo.23018. [PubMed: 30098276]

Wosiski-Kuhn M, Erion JR, Gomez-Sanchez EP, Gomez-Sanchez CE, Stranahan AM. Glucocorticoid receptor activation impairs hippocampal plasticity by suppressing BDNF expression in obese mice. Psychoneuroendocrinology. 2014 Apr;42:165–77. [PubMed: 24636513]

Yamamoto M, Guo DH, Hernandez CM, Stranahan AM. Endothelial Adora2a Activation Promotes Blood-Brain Barrier Breakdown and Cognitive Impairment in Mice with Diet-Induced Insulin Resistance. J Neurosci. 2019 May 22;39(21):4179–4192. [PubMed: 30886019]

Research Highlights

- Intrahippocampal delivery of the tamoxifen metabolite Z-endoxifen enables region-specific genetic manipulation of glial cells
- Intrahippocampal administration using microfluidic polymer fibers elicits widespread recombination with less damage than steel cannulas
- Glial reactivity was further minimized when polymer fiber devices were implanted and allowed to acclimate for extended periods before drug delivery

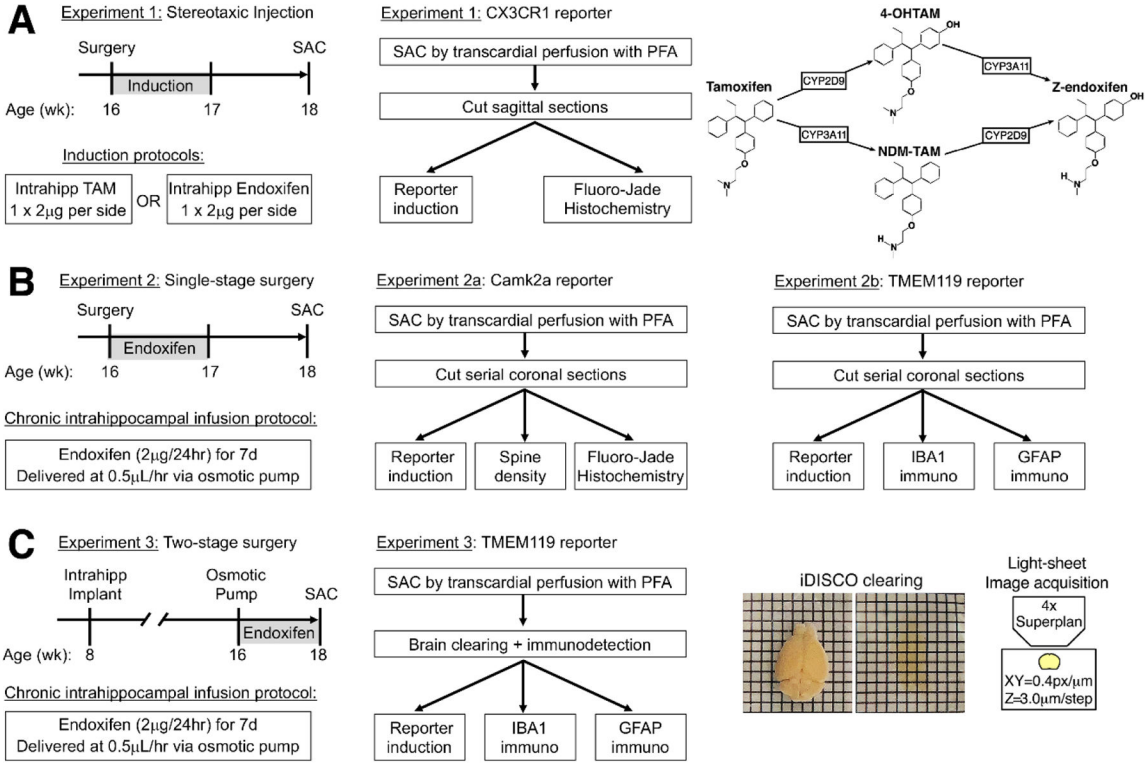

Figure 1. Experimental design.

(A) In Experiment 1, reporter induction and cellular degeneration were assessed in CX3CR1^{creERT2}/tdTomato$^{fl/fl}$ mice after intrahippocampal injections of tamoxifen or Z-endoxifen. Far right schematic depicts hepatic breakdown of tamoxifen (TAM), generating endoxifen and other metabolites. Abbreviations: 4OHTAM, 4-hydroxy-tamoxifen; NDM-TAM, N-desmethyl-tamoxifen; PFA, paraformaldehyde; SAC, sacrifice. (B) In Experiment 2, chronic intrahippocampal infusions of endoxifen were carried out using steel cannulas or microfluidic polymer fibers attached to osmotic minipumps. Infusion devices were implanted in a single surgery ('Single-stage surgery') using (2) distinct transgenic lines. Neurodegeneration, reporter induction, and synaptic structure were analyzed after chronic infusions in CaMK2a^{creERT2}/tdTomato$^{fl/fl}$ mice. Gliosis and reporter induction were analyzed after stereotaxic injection or chronic infusions in microglia-specific TMEM119^{creERT2}/tdTomato$^{fl/fl}$ mice. (C) In Experiment 3, TMEM119^{creERT2}/tdTomato$^{fl/fl}$ mice received intrahippocampal implants at 8wk old, with a second surgery to connect osmotic minipumps for endoxifen infusions at 16wk old ('Two-stage surgery'). Gliosis and reporter induction were analyzed in cleared brains using light-sheet microscopy (far right panel).

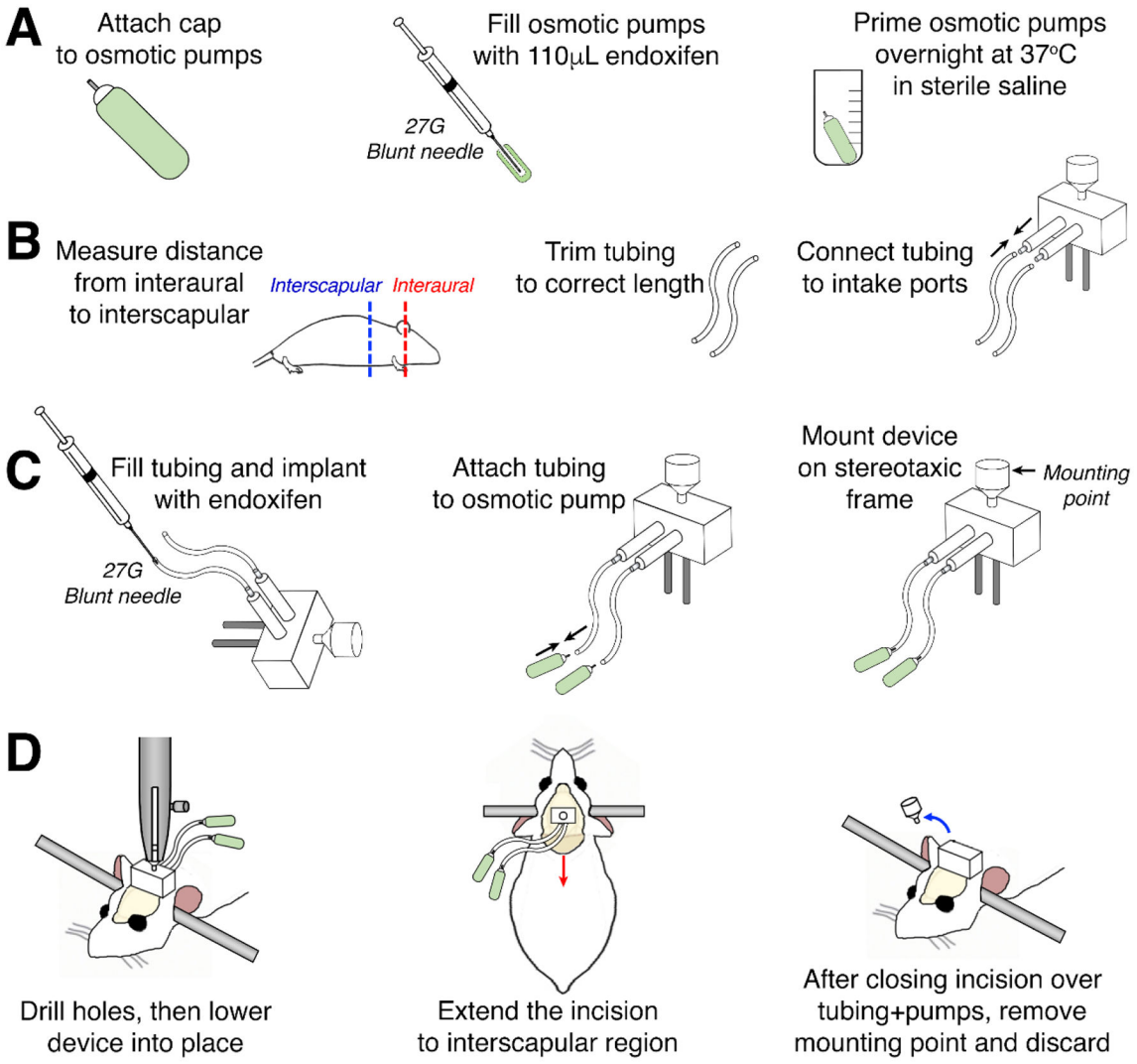

Figure 2. Device assembly and surgical overview.

(A) Attach flow moderator cap to osmotic pump (left). Fill pumps with endoxifen using a 1cc syringe with 27g blunt needle (middle). Prime pumps overnight in sterile saline (right). (B) Estimate distance from the interaural line to interscapular region, then add 1.5-2.0cm to allow for movement of the head (left). Trim segments of polyethylene tubing to the correct length (middle). Connect polyethylene tubing to intake ports on the cannula base (right). (C) Fill tubing and cannula with endoxifen (left). Attach tubing to flow moderator cap on osmotic pump (middle). Mount infusion device on a stereotaxic frame using the tab on top of the cannula (right). (D) Drill holes, then lower device into place and secure with dental cement (left). Extend the scalp incision to the interscapular region, then insert tubing and pumps under the skin (middle). Remove the mounting tab on top of the cannula and discard (right). Steps in (A-B) can be carried out the day before surgery. Steps in (C-D) should be carried out in a sterile area adjacent to the surgical site to avoid introduction of bubbles. For all panels, drawings are not to scale (see Supplementary Fig.1 for dimensions).

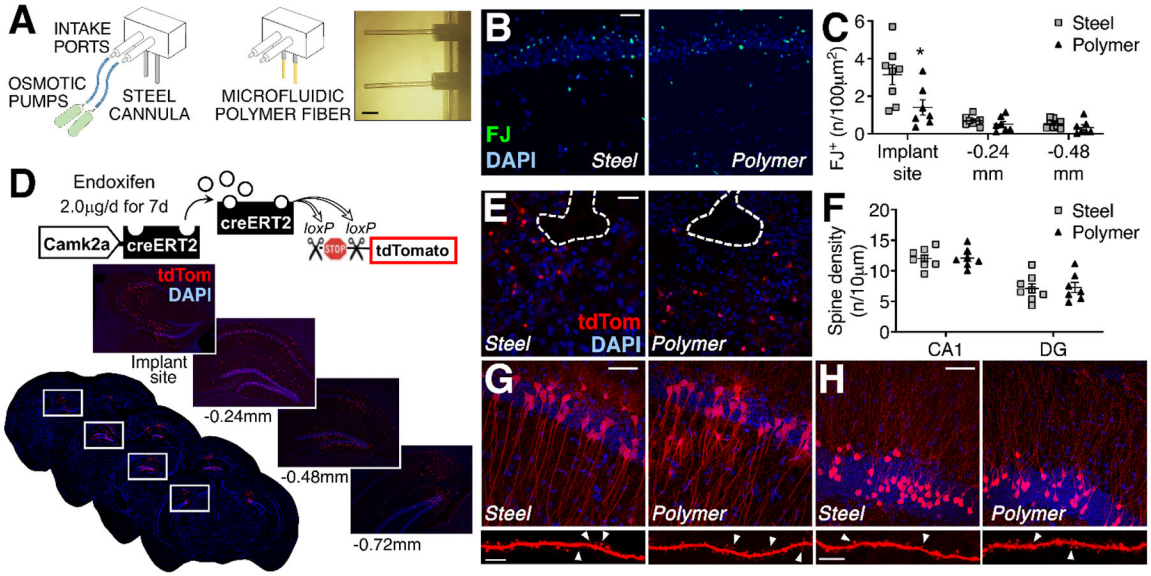

Figure 3. Local recombination following intrahippocampal delivery of endoxifen.

(A) Left panels show tiled epifluorescence micrographs of native tdTomato fluorescence 1wk after intrahippocampal injections of ACSF, endoxifen, or tamoxifen (TAM; scalebar=1.0mm). Right panels show high-magnification images of tdTomato in the hippocampus (scalebar=10 microns). (B) Graph shows tdTomato+ cell counts after endoxifen, ACSF, or TAM; inset shows values after intrahippocampal ACSF or TAM. (C) Stereotaxic injection is accompanied by localized tissue damage, based on Fluoro Jade (FJ) staining after intrahippocampal ACSF, endoxifen, or TAM. Scalebar=25 microns. (D) Similar numbers of FJ+ nuclei in hippocampal area CA1 after stereotaxic injections of endoxifen, ACSF, or TAM. Each symbol represents (1) mouse, line height shows group mean, and error bars show SEM (n=6/condition). Asterisk indicates significant difference at $p<0.05$ by one-way ANOVA with Tukey's post hoc.

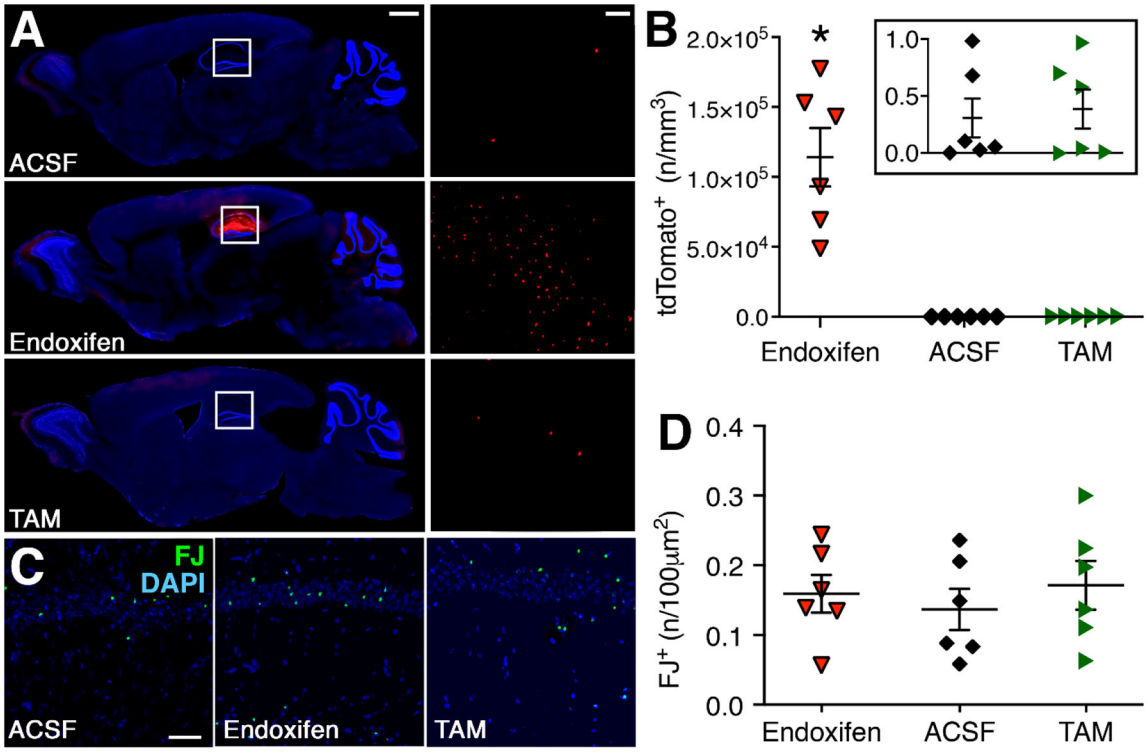

Figure 4. Chronic intrahippocampal delivery of endoxifen via microfluidic polymer fibers limits neuronal damage at the implant site.

(A) Bilateral steel cannulas were attached to osmotic pumps and microfluidic polymer fibers (right) were inserted into 'stub' cannulas and trimmed before assembly. Inset shows trimmed fibers (scalebar=0.5mm). (B) Fluoro Jade (FJ) histochemistry 2wk after implantation of steel cannulas (Steel) or polymer fiber implants (Polymer). Micrographs show implant site, scalebar=25 microns. (C) Stereological quantification of FJ-stained nuclei on serial coronal sections revealed fewer degenerating neurons around the implant site in mice with polymer fiber implants. (D) Schematic (top panel) shows design for chronic intrahippocampal infusion of endoxifen in Camk2a^{creERT2} reporter mice. Implant sites were identified based on tdTomato (tdTom) expression and DAPI counterstain. (E) tdTom+ cells at the implant site lacked processes and exhibit nuclear condensation. (F) Analysis of dendritic spine density in CA1 and dentate gyrus (DG) distal to the implant site (>0.24mm) revealed no effect of implant material. (G-H) Normal cellular morphology and representative dendritic segments from the CA1 stratum radiatum (G) or dentate molecular layer (H) in each condition. Arrowheads shown with dendritic segments indicate spines; scalebar shown with segments = 5.0 microns; all other scalebars = 25 microns. For graphs, each symbol represents (1) mouse, line height shows group mean, and error bars show SEM (n=6-8 mice/condition). Asterisk (*) indicates $p<0.05$ by one-way ANOVA.

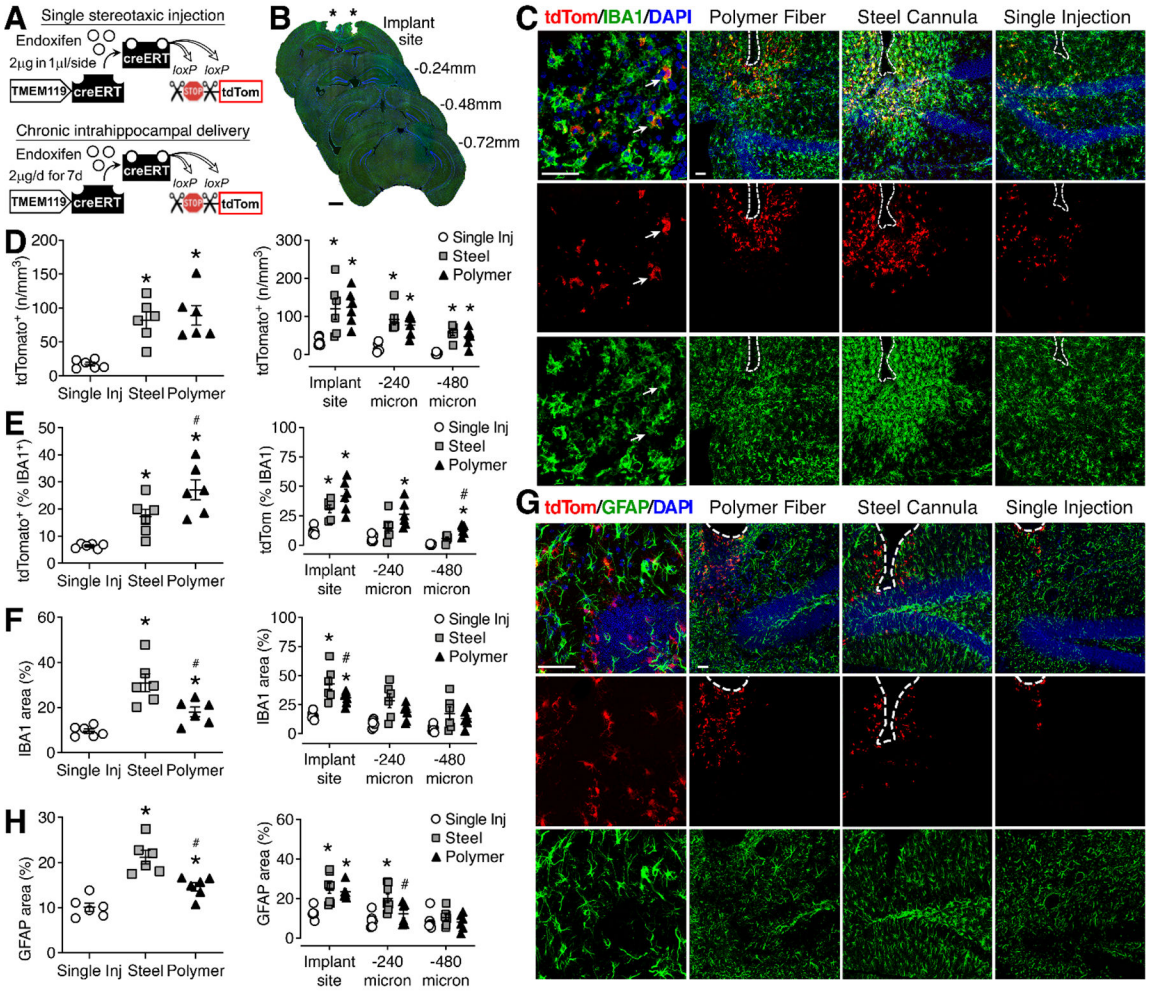

Figure 5. Reporter induction and glial reactivity after chronic intrahippocampal endoxifen via steel cannulas or microfluidic fibers.

(A) Experimental design for stereotaxic injection or chronic intrahippocampal delivery of endoxifen in TMEM119^{creERT2}/tdTomato$^{fl/fl}$ mice. (B) Native tdTomato (tdTom) fluorescence and IBA1 immunoreactivity were visualized in serial coronal sections after single stereotaxic injection or chronic intrahippocampal delivery. Asterisks indicate placement sites on tiled epifluorescence images, scalebar (bottom left)=1.0mm. (C) Colocalization between IBA1 and tdTom on confocal z-stacks (arrows indicate double-labeled cells). (D) Chronic delivery of endoxifen via polymer fiber implants (Polymer) or steel cannulas (Steel) elicits more widespread reporter induction than single stereotaxic injection (Single Inj). Left graph shows tdTomato+ cell numbers across all distances from the implant site; right graph shows cell counts binned by distance. (E) When co-labeling was averaged across all distances from the implant site (left graph), mice that received polymer fiber implants had significantly more double-labeled cells than mice with steel implants. This effect was most prominent at regions distal to the implant site (right graph). (F) Increases in IBA1 immunoreactivity are less pronounced after implantation of polymer fibers, relative to steel cannulas, based on aggregate data from serial sections (left) and analysis at intervals relative to the implant site (right). (G) Z-projections (right)

revealed thicker astroglial processes but no colocalization between GFAP and tdTomato in TMEM119^{creERT2}/tdTomato$^{fl/fl}$ mice; lower-power micrographs show representative GFAP immunoreactivity in each condition. (H) Increases in GFAP immunoreactivity are less widespread after delivery via polymer fibers, relative to steel cannulas, as determined by analysis of serial sections (left) and comparisons binned by distance (right). For all graphs, each symbol represents (1) mouse, line height shows group mean, and error bars show SEM (n=6 mice/condition). Asterisk indicates effect of chronic delivery and hashtag indicates differences between steel and polymer at $p<0.05$ by ANOVA with Tukey's post hoc.

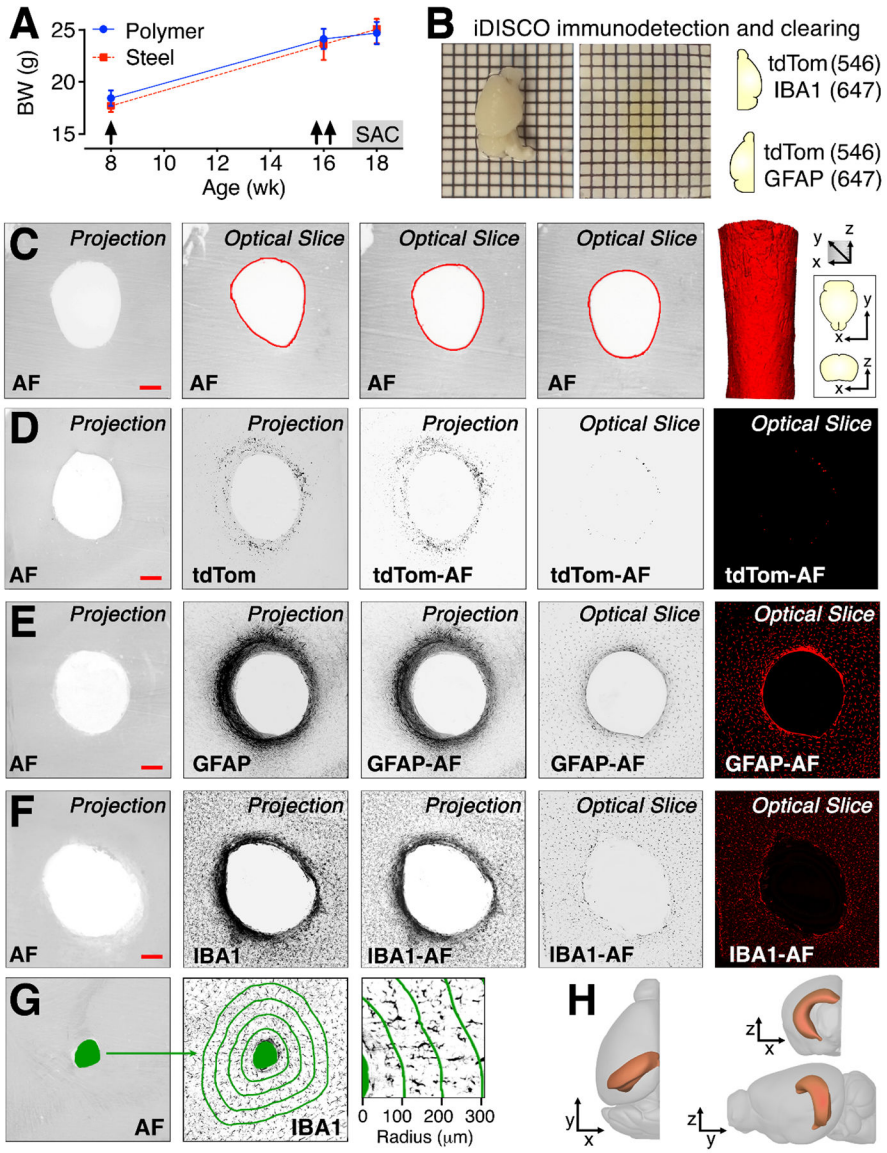

Figure 6. Methods for imaging and analysis of cleared brains after two-stage implantation of delivery devices and osmotic pumps.

(A) Graph shows weight gain after implantation of microfluidic polymer fibers or steel cannulas (single arrow), 8wk before infusion via osmotic pumps (double arrow) in TMEM119^{creERT2}/tdTomato$^{fl/fl}$ mice. There was no effect of device material on weight gain before or after infusions. (B) Solvent-based sample clearing using iDISCO (grid=2.0mm) and fluorophores used for immunodetection. (C) Autofluorescence (AF) images were acquired from all samples, stitched, and used for 3D reconstruction of the cannula track (far right panel; scalecube=200 microns in XYZ). (D) Autofluorescence images were subtracted from images of tdTomato (tdTom); after subtraction, stitched z-stacks were thresholded for algorithmic quantification of labeled cells. (E-F) Images of GFAP (E) or IBA1 (F) were acquired in parallel with images of tdTomato in each sample. After stitching and autofluorescence correction, z-stacks were thresholded for analysis of suprathreshold staining area. (G) For Sholl analysis, 2D traces of the cannula track

(green solid region) from autofluorescence images (AF) were overlaid on corresponding images of IBA1. The boundaries of the initial tracing were scaled up in 100 micron increments, generating concentric traces (green outlines) around the cannula track. Adjacent pairs of traces were used to delineate regions of interest (ROIs) for analysis of IBA1 immunoreactivity. (H) Group differences were determined within the boundaries of the hippocampus (orange shaded region) after registration onto the Allen Brain Atlas Common Coordinate Framework.

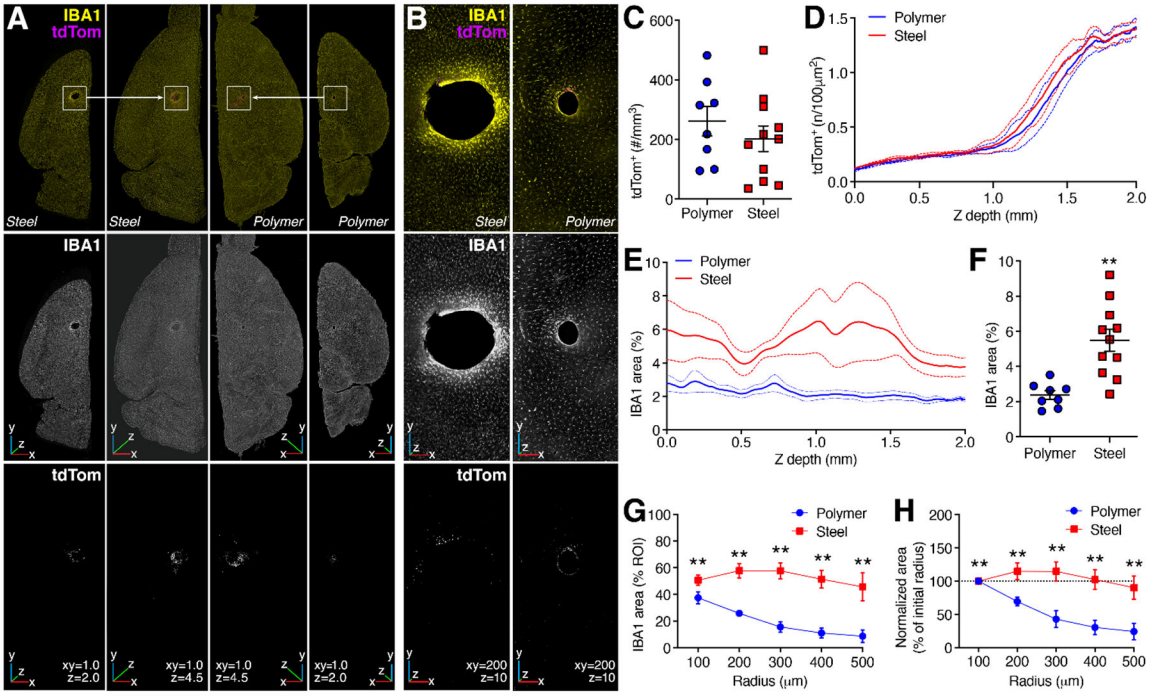

Figure 7. Light-sheet imaging of microgliosis and tdTomato induction after two-stage surgery.

(A) Tiled z-stack images of IBA1 and tdTomato (tdTom) were captured in cleared brains from TMEM119creERT2/tdTomatofl/fl mice, 2wk after intrahippocampal delivery of endoxifen via steel cannulas (Steel) or microfluidic polymer fibers (Polymer). For panels (A-B), middle row shows single channel images of IBA1 and bottom row shows tdTom. Scalebar lengths in (A) are in mm; scalebar lengths in (B) are in microns. (B) Native resolution images of IBA1 and tdTom. (C) No effect of implant material on the number of tdTom+ cells. (D) No evidence of differential backflow after chronic intrahippocampal infusion of endoxifen via steel cannulas or microfluidic polymer fibers. Z-depths shown on the X-axis in panels (C,E) indicate dorsoventral position (0=cortical surface). (E) Analysis of IBA1 staining at the implant site revealed increased immunoreactivity around steel cannulas, irrespective of depth. (F) Differences in IBA1 staining area were also evident when immunoreactivity was averaged over the entire length of the cannula. (H) IBA1 immunoreactivity declines as a function of distance around polymer fiber implants, but remains elevated at comparable intervals around the border of steel cannula tracks. (I) The same pattern is evident after normalizing IBA1 labeling area in distal ROIs to values from the initial toroid (0-100 microns around the track). For panels (C,F), symbols represent (1) mouse; for all other graphs, symbols or solid lines represent the mean of (n=8) mice/condition. Error bars in all graphs represent SEM. Asterisk indicates significant difference between steel and polymer probes at $p<0.05$ by t-test (D-F) or repeated-measured ANOVA with Tukey's post hoc (H-I).

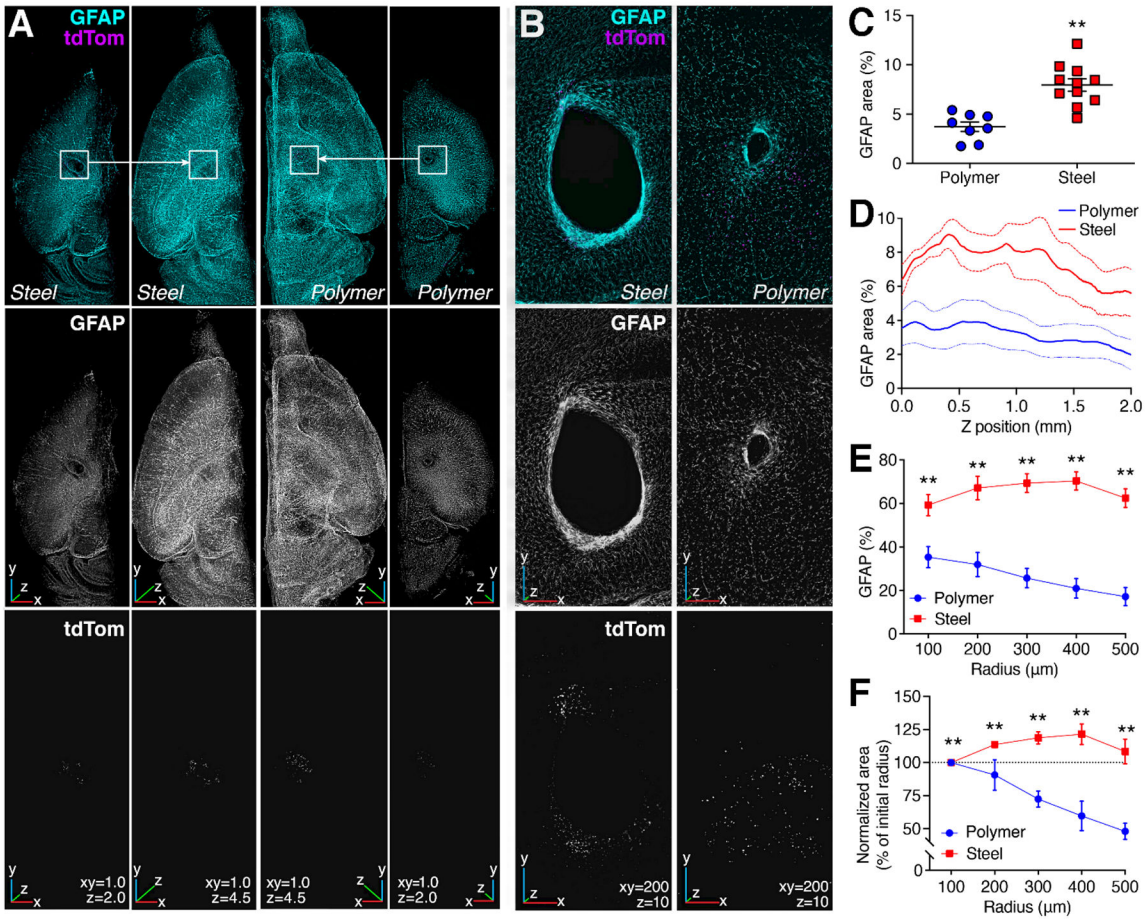

Figure 8. Astrogliosis and reporter expression after two-stage surgery.

(A-B) Tiled z-stack images of GFAP and tdTomato (tdTom) were acquired in cleared brains from mice with bilateral steel cannulas (Steel) or polymer fiber implants (Polymer). Middle row shows single channel images of GFAP and bottom row shows tdTom. For panel (A), scale bar lengths are in mm. (B) Native resolution images of GFAP and tdTom. Scaling information (bottom) is in microns. (C) Increased GFAP immunoreactivity around steel cannulas, relative to polymer fibers. (D) Differences in GFAP labeling were evident over the entire dorsoventral length of the implant; solid lines show the average of (n=8) mice/condition and dashed lines represent SEM. (E) GFAP immunoreactivity declines at greater distances from polymer fiber implants, but not steel cannulas. (F) Distance-dependent changes in GFAP labeling persist after normalization to staining in the initial toroid (0-100 microns) around each track. For panels (D-E), symbols represent (1) mouse; for (E-F), symbols represent the mean of (n=8) mice/condition. Error bars in all graphs represent SEM. Asterisks indicates significant difference between steel and polymer probes at $p<0.05$ by t-test (D-F) or by repeated-measured ANOVA with Tukey's post hoc (H-I).